J. Fluid Mech. (1990), *vol.* 213, *pp.* 267–286
Printed in Great Britain

Effect of Reynolds number on the topology of the organized motion in a turbulent boundary layer

By R. A. ANTONIA, D. K. BISSET AND L. W. B. BROWNE
Department of Mechanical Engineering, University of Newcastle, N.S.W., 2308, Australia

(Received 5 September 1988 and in revised form 4 September 1989)

The influence of Reynolds number on the topology of the organized motion in a turbulent boundary layer is studied with the use of an array of eight ×-probes in the plane of mean shear. Instantaneous sectional streamlines and contours of large-scale approximations to the spanwise vorticity and strain rate suggest that the motion is relatively complicated at all Reynolds numbers. Contours, conditioned on the spatially coherent increase in the velocity fluctuation u, extend to larger distances from the wall at the smaller Reynolds numbers. Reasonable correspondence is found between the location of this increase in the near-wall region and the end of a burst. Associated with this increase is an important contribution to the Reynolds shear stress throughout the layer. This contribution is larger at the smaller Reynolds numbers.

1. Introduction

The effect of Reynolds number on the wall and outer regions of a turbulent boundary layer has been considered by a number of investigators using different approaches. The earlier work of Coles (1962) provided a measure of the effect of R_θ (the Reynolds number based on the free-stream velocity and the momentum thickness θ) on the 'strength of the wake', represented by the maximum departure, $\Delta\bar{U}_{\max}/U_\tau$, from the log law. The effect of R_θ on both mean velocity and Reynolds stress distributions has been established by several authors (e.g. Purtell, Klebanoff & Buckley 1981; Subramanian & Antonia 1981; Murlis, Tsai & Bradshaw 1982; Antonia *et al.* 1982; Andreopoulos *et al.* 1984; Erm, Smits & Joubert 1987) using hot-wire anemometry. Although there are differences of detail, there is general consensus among these investigations that the major Reynolds number effects only occur when R_θ is less than about 3000.

Effective use has been made of flow visualization to study the large-scale features of boundary-layer flows. In the wall region, approximate independence on R_θ has been found for the low-speed streaks (Smith & Metzler 1983). In the outer region, Falco (1974) and Head & Bandyopadhyay (1981, hereafter referred to as HB) have shown that structural features are affected by R_θ somewhat more emphatically than indicated by hot-wire measurements. HB described the influence of R_θ in the context of vortex loops or hairpin vortices originating in the wall region and extending throughout the layer with an inclination of about 45° to the wall. For $R_\theta \lesssim 800$, the description is in terms of vortex loops, while random arrays of highly elongated hairpin vortices prevail for $R_\theta \gtrsim 2000$. These authors also indicated that the hairpin-like vortex description is consistent with the observed temperature front (the sharp decrease in temperature or cooling (Chen & Blackwelder 1978) that sometimes extends from just outside the viscous sublayer to almost the edge of the boundary

layer; see also Subramanian *et al.* 1982). While the sawtooth trip used by HB undoubtedly emphasized the organization of the hairpin vortices, Wallace *et al.* (1983), using smoke flow visualization and several types of trips, as well as no trip, have indicated that the existence of hairpin-like vortical structures is not in question. Confirmation of these structures was provided by the smoke visualization of Falco (1980) and Wallace (1984), the latter noting that, as R_θ increased, the features changed scale but not character.

It should be noted, parenthetically, that a criticism often levelled at smoke visualization is that the Schmidt number of smoke is high (of order 10^4). Thus, although vorticity is diffused rapidly by viscosity, smoke is diffused relatively slowly by molecular action. There is therefore a tendency for the smoke to maintain its patterns longer than the actual flow patterns are maintained, particularly at low R_θ. This is a major difficulty, for example when smoke is used to detect the turbulent/non-turbulent interface. Falco (1977), however, also noted that the Schmidt number argument is not a limiting one as far as the motion which carries the Reynolds stress is concerned, the timescale of this motion being much smaller than the molecular diffusion timescale. While smoke cannot mark all vortical regions accurately, there is no reason for doubting the existence of vortical structures inferred from smoke photographs and films (see, for example, Falco's (1980) comparison between smoke-marked typical eddies and simultaneous traces of u and v). In the smoke visualizations of Wallace *et al.* (1983) and Wallace (1984) the Schmidt number effect was minimized by: (i) seeping the smoke into the sublayer just upstream of the field of view (and not at the beginning of the boundary layer as in HB; and (ii) marking the outer edge of the layer by smoke introduced (into the free stream) at an upstream location such that it intercepted the outer edge at the beginning of the field of view.

Direct numerical simulations of the boundary layer have been carried out by Spalart (1988) at four Reynolds numbers in the range $R_\theta = 255$ to 1410. This is a range in which one would expect relatively important Reynolds number effects and this is indeed what the simulations indicate. In particular, in the near-wall region, the magnitudes of all the Reynolds stresses increase systematically with R_θ.

The use of an array of $\times$-probes suitably located in the boundary layer allows flow patterns to be visualized and interpreted less ambiguously than in flow visualization experiments. This approach was recently adopted by Antonia, Browne & Bisset (1989), hereafter referred to as I, who used eight $\times$-probes in the (x, y) plane, where x is in the flow direction and y is normal to the surface, to initiate a study of the topology of the large-scale motion. A detailed study was made in I of the effect of R_θ on space–time correlations of u and v; isocorrelations of u were found to be more affected by R_θ than those of v, apparently reflecting the difference in lengthscales with which u and v are associated. There was negligible dependence on R_θ of the correlations for $R_\theta \gtrsim 5000$. The main aim of the present paper is to extend the topological study commenced in I with a view to assessing the influence of R_θ on flow patterns characterized by streamlines and isocontours of the spanwise vorticity and the strain rate. A second aim is to gain some insight into the relationship between the outer motion and near-wall bursting, and the possible influence of R_θ on this relationship, especially with respect to uv.

2. Experimental details and conditions

The wind tunnel is of the open-return blower type; a double inlet centrifugal blower is followed by a diffuser, settling chamber (containing a honeycomb and a number of screens), a 6 to 1 two-dimensional contraction and a 5.4 m long working section with a height of 0.89 m and a width of 0.15 m at the exit from the contraction. As shown in figure 1, the boundary layer develops on one of the walls of the working section, the opposite wall being tilted to maintain a zero pressure gradient for a particular free-stream velocity U_1. Details of the boundary-layer trip as well as a definition of the co-ordinate axes are given in figure 1.

Measurements were made using an array of 8 ×-probes, shown schematically in figure 1, aligned in the y-direction (normal to the wall) at the same x- and z-locations. The distance between adjacent ×-probes is approximately constant, equal to about 5 mm. The 5 μm diameter hot wires were etched from Wollaston (Pt–10 % Rh), the length to diameter ratio of each wire being about 250. The wires were operated with constant-temperature circuits, built in-house, at an overheat of 0.6. Output signals from these circuits were passed through buck and gain circuits and then low-pass filtered before digitizing into a PDP 11/34 computer. The filter cut-off frequency was 1750 Hz for each channel. The sampling frequency was 3000 Hz (per channel), the maximum value attainable with the present 16 channel, 12 bit data acquisition system. The difference between the sampling frequency and the Nyquist frequency (3500 Hz) is unlikely to affect any of the results of the present investigation, which is primarily concerned with relatively large-scale features of the flow. Digital data files of approximately 50 s duration were stored on magnetic tape and processed on a VAX 8550 computer.

The array was traversed across the boundary layer using a mechanism with a least count of 0.01 mm. The initial distance of the ×-probe nearest the wall was determined using the reflection method and a theodolite. Velocity and yaw calibrations of the ×-probes were done in the free stream using a data logger–personal computer combination. The data logger was operated at a sampling frequency of 10 Hz. For calibrations, a Pitot tube located in the free stream was connected to a Baratron transducer.

As a check of the performance of the ×-probes (each with a nominal included angle of 90°) in the near-wall region, where the local turbulence intensity $\overline{u^2}^{\frac{1}{2}}/\bar{U}$ becomes important, the root-mean-square value of the velocity vector angle β, where $\beta = \tan^{-1}[v/(u+\bar{U})]$, was calculated. The calculation was made for the ×-probe nearest the wall (y/δ is approximately 0.025 for all R_θ). It was found that $\overline{\beta^2}^{\frac{1}{2}}$ was typically in the range 5°–6°, the lowest and highest values of β being $-30°$ and $+33°$ respectively. The latter range suggests that fluctuations of the velocity vector in the (x, y)-plane should be adequately resolved by an ×-probe with a 90° included angle. The above values for $\overline{\beta^2}^{\frac{1}{2}}$ are consistent with those presented in Browne, Antonia & Chua (1989).

Measurements were made at a distance x of 4.3 m at four values of U_1: 3, 4.2, 10.9 and 19.7 m/s. The corresponding values of the momentum-thickness Reynolds number R_θ are 1360, 2180, 6030 and 9630. Mean flow characteristics at these Reynolds numbers are summarized in table 1. The table also shows the values of y^+ corresponding to $y = 1.5$ mm, the location of the ×-probe closest to the wall. Tests which demonstrated the satisfactory performance of the hot wires are reported *in I* and will not be discussed here. We shall just note that the tabulated values of

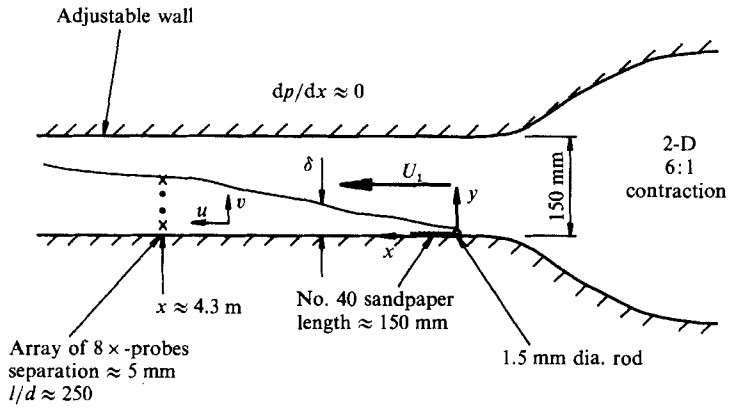

FIGURE 1. Schematic arrangement of wind-tunnel working section and layout of sensors.

$\Delta\bar{U}_{max}/U_\tau$ are in reasonable agreement with those of Coles (1962), indicating a normal evolution of the boundary layer.

Profiles of the Reynolds normal stresses, normalized by U_τ^2 and plotted against y/δ (figure 2*a*, *b*), show that there is practically no difference between the two highest Reynolds numbers. The influence of R_θ is confined to $R_\theta = 1360$ and 2180 and this is more pronounced for $\overline{u^2}/U_\tau$ than $\overline{v^2}/U_\tau$. The noticeable differences between the present $\overline{u^2}$ values at $R_\theta = 1360$ and those of Erm *et al.* (1987) must be attributed to the considerably different wind-tunnel conditions. In order to obtain different R_θ values, Erm *et al.* (1987) varied the downstream location of measurement and the size of the trip as well as the free-stream velocity. The distributions of $-\overline{uv}/U_\tau^2$ (figure 2*c*) at the two largest values of R_θ are in reasonable agreement with each other and with Klebanoff's (1955) distribution ($R_\theta \approx 8000$). Reasonable agreement is also observed for the two smallest values of R_θ but these distributions fall below those at the larger Reynolds numbers in the outer layer and rise above them in the inner region. In this sense, the behaviour of the data in figure 2(*c*) is in closer qualitative agreement with that of Murlis *et al.* (1982) or Erm *et al.* (1987) than Subramanian & Antonia (1981). Spalart (1988) attributed the influence of R_θ on the normal Reynolds stresses to the large-scale 'inactive' motion; this association is not entirely consistent with the effect of R_θ on $-\overline{uv}$, as reported by Spalart and observed in figure 2(*c*), since, by definition, the inactive motion should not produce any shear stress in the near-wall region.

3. Flow topology

The data from the ×-probe array can be used to display the instantaneous velocity vector field in the plane of the array. An example is shown in figure 3(*a*) where velocity vectors corresponding to $R_\theta = 1360$ are shown in a frame of reference which translates at a constant convection speed U_c, equal to $0.8U_1$. This velocity has been used by other authors (Brown & Thomas 1977; Robinson, Kline & Spalart 1989) to display instantaneous and conditional velocity vectors in the (x, y)-plane. Polynomial interpolation in the y-direction has been used to add two extra lines of data per probe, and the interpolated data are used in all figures that show sectional streamlines, vorticity, or strain rate. The x velocity component is $u + \bar{U} - U_c$ while the y velocity component is v (the mean velocity $\bar{V}$ was negligible). The horizontal

U_1 (m/s)	R_θ	c_f present (Preston tube)	c_f Coles (1962)	δ (mm)	δ^* (mm)	θ (mm)	$\frac{\Delta\bar{U}_{max}}{U_\tau}$ present	$\frac{\Delta\bar{U}_{max}}{U_\tau}$ Coles (1962)	y^+ or l^+ (corresp. to $y = l = 1.5$ mm)
3	1360	0.0040	0.0040	59	10	6.8	1.5	1.8	13.4
4.2	2180	0.0034	0.0036	68	11	7.8	1.7	2.2	17.3
10.9	6030	0.0029	0.0029	66	11.6	8.3	2.8	2.8	41.5
19.7	9630	0.0027	0.0026	64	9.9	7.3	2.8	2.7	72.4

TABLE 1. Mean velocity characteristics

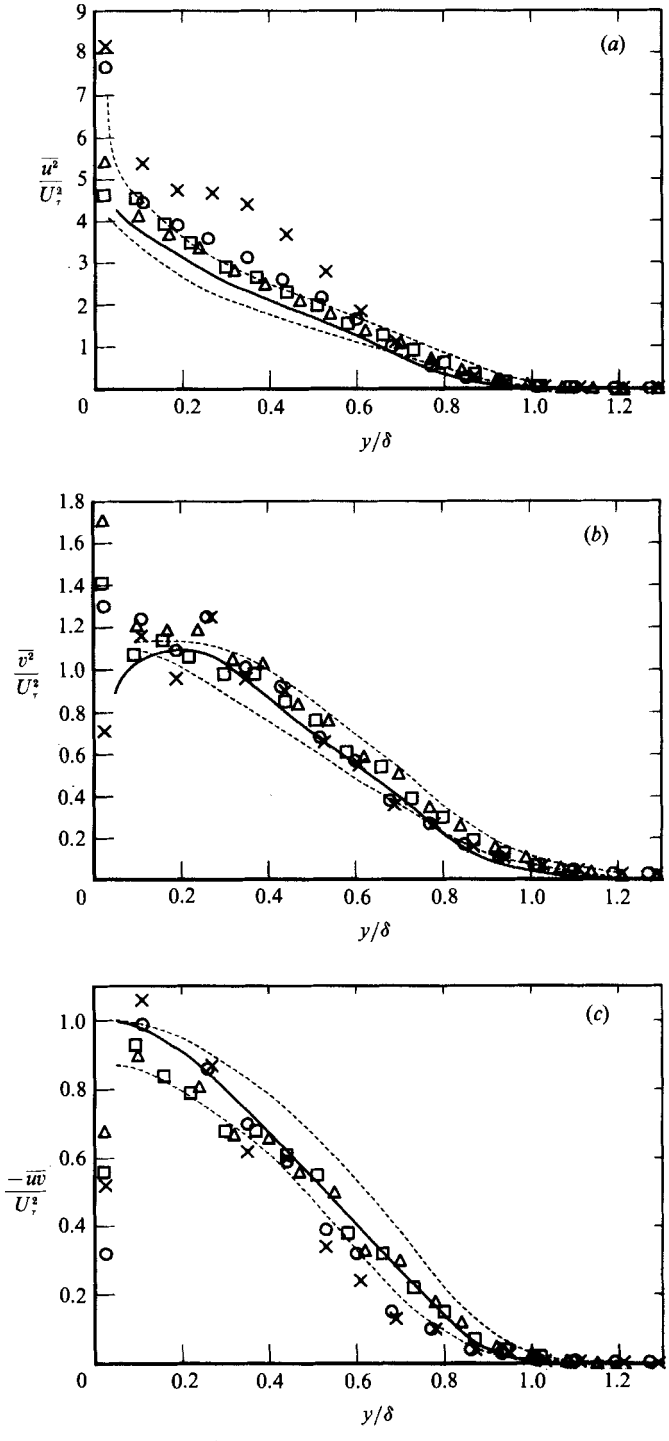

FIGURE 2. Reynolds stress distributions: ×, $R_\theta = 1360$; ○, 2180; △, 6030; □, 9630. – – –, limits of the Erm *et al.* (1987) data; ——, Klebanoff (1955), $R_\theta \approx 8000$. (*a*) $\overline{u^2}/U_\tau^2$; (*b*) $\overline{v^2}/U_\tau^2$; (*c*) $-\overline{uv}/U_\tau^2$.

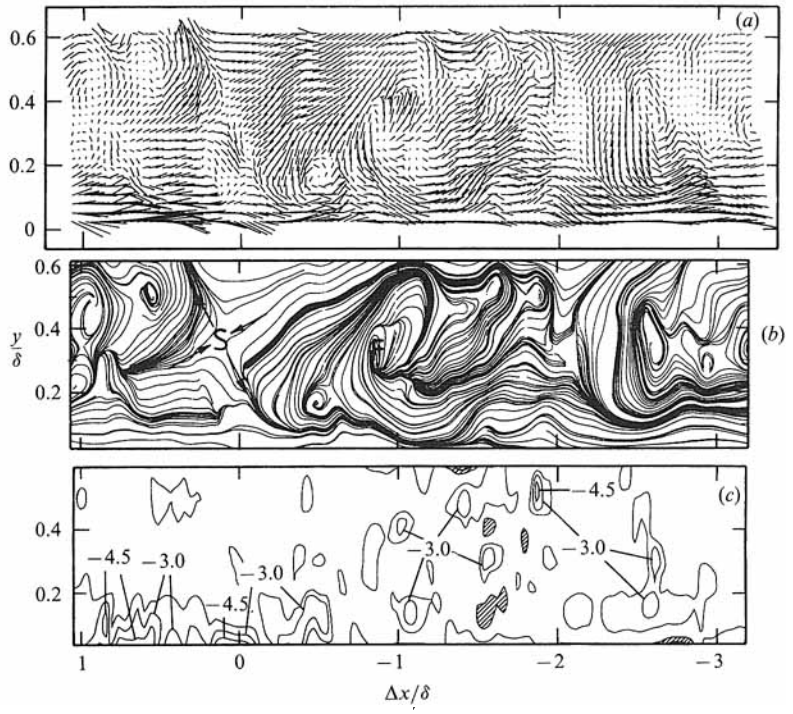

FIGURE 3. (*a*) Instantaneous velocity vectors, (*b*) sectional streamlines and (*c*) contours of approximate spanwise vorticity $\omega_z\delta/U_1$ calculated from the vectors in (*a*). The information is viewed in a frame of reference which translates to the left with $U_c = 0.8U_1$. $R_\theta = 1360$. Note: hatched contours have a value of $+1.5$. Unlabelled contours have a value of -1.5.

scale $\Delta x/\delta$ has been obtained by multiplying time with $-U_c/\delta$. Although the selection of a constant U_c is arbitrary, it may be reasonable in the present context, since the main aim is to provide a qualitative comparison of features at different R_θ.

Sectional streamlines, as defined by Perry & Chong (1987), are obtained by integrating the measured velocity components in the (x, y)-plane. For brevity, sectional streamlines will hereafter be referred to as streamlines. The streamlines in figure 3(*b*) contain two types of critical points (saddles and foci; one example of each is labelled in the figure) at which the velocity is zero and the streamline slope is indeterminate.

The spanwise vorticity ω_z (figure 3*c*) can be calculated from the U- and V-data using the approximation $\omega_z \approx -\bar{U}^{-1}\partial V/\partial t - \partial U/\partial y$ on the interpolated data. The calculated values of ω_z are smoothed and attenuated due to the y-separation between the ×-probes. These values should therefore only be interpreted as approximations to the spanwise vorticity associated with a relatively large-scale motion (e.g. Hussain 1986) rather than point measurements of ω_z. We have verified that this calculation is unaffected when $\bar{U}$ is replaced by U_c, provided U_c is within the range of $\bar{U}$-values, and Taylor's hypothesis has recently been validated above the buffer layer by Piomelli, Balint & Wallace (1989). The velocity vectors and streamlines depend, however, on the choice of U_c (e.g. Coles 1982; Hussain 1986; Kim 1985; Perry & Chong 1987). Comparison between figures 3(*b*) and 3(*c*) reveals that, away from the wall, foci of fairly small spatial extent correspond approximately with local regions of concentrated spanwise vorticity. Although this coincidence provides some

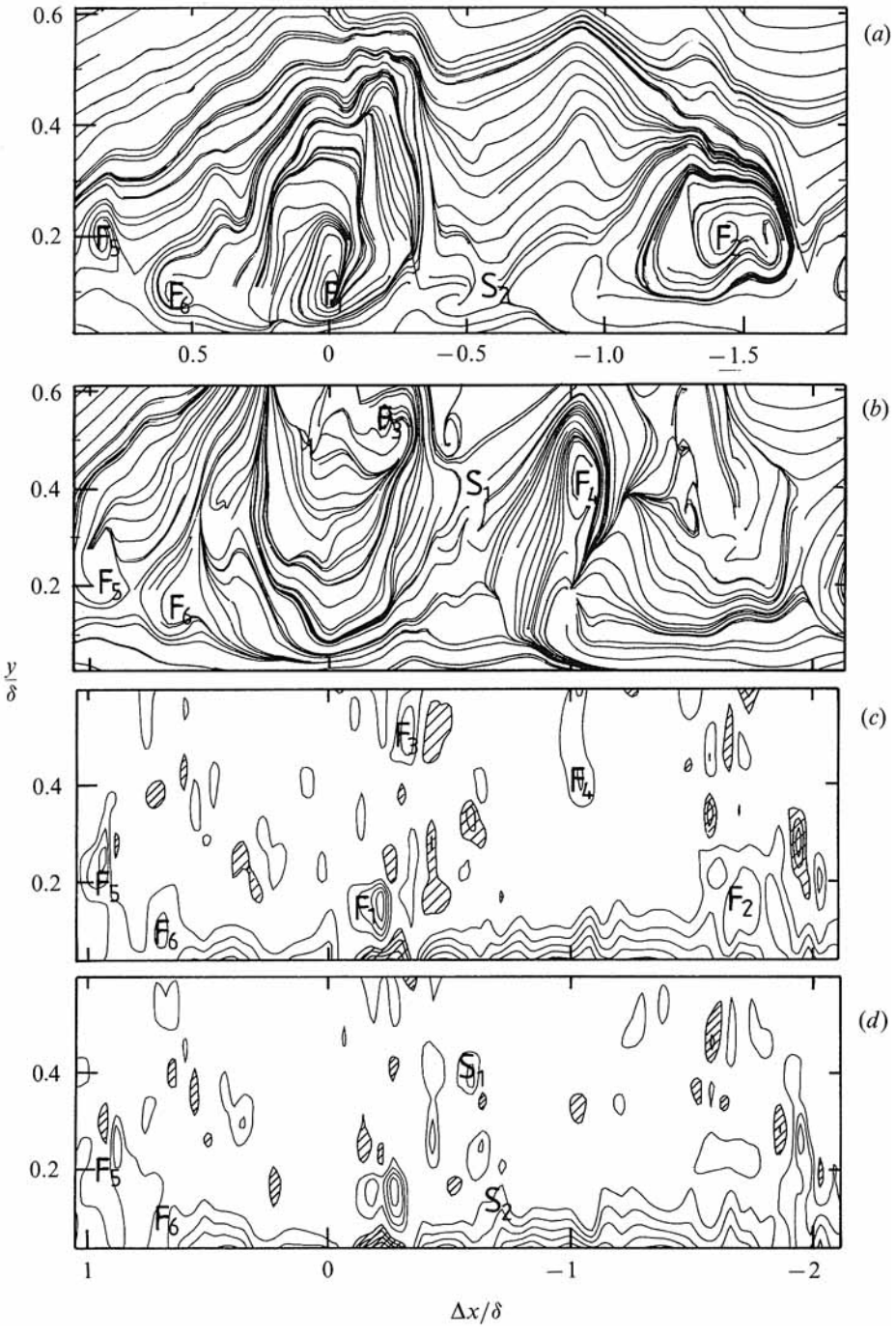

FIGURE 4. Comparison between sectional streamlines for two choices of the convection velocity (*a*) $U_c = 0.7U_1$, (*b*) $0.8U_1$; (*c*) contours of large-scale spanwise vorticity ω_z (hatched is positive); and (*d*) strain rate γ (hatched is negative), for $R_\theta = 1360$. Flow is to the left. Contour values: $\pm 1.5, \pm 3, \ldots$.

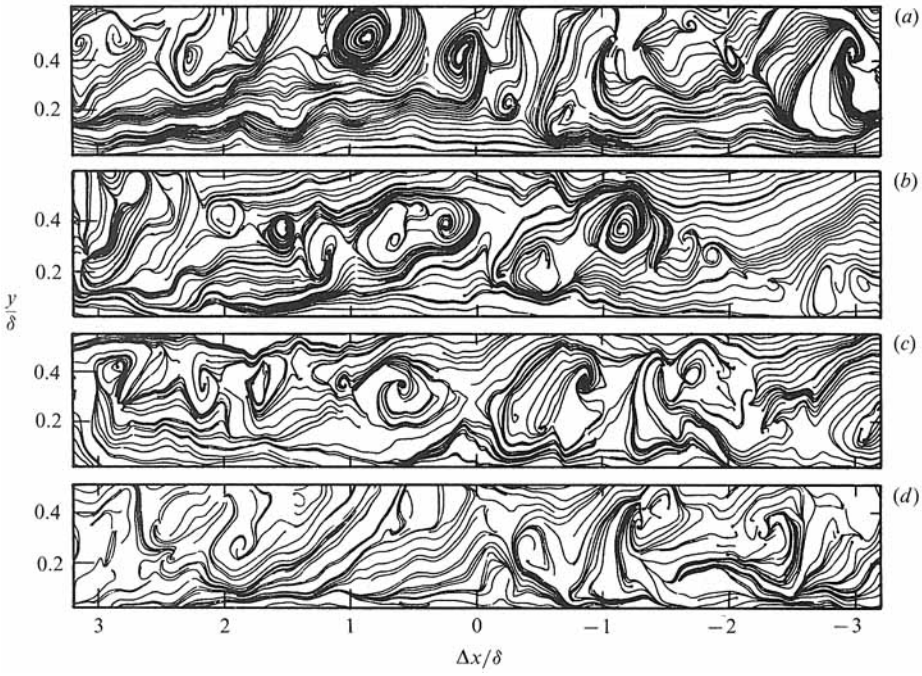

FIGURE 5. Instantaneous sectional streamlines in a frame of reference translating to the left with a velocity $U_c = 0.8U_1$ for different Reynolds numbers. (*a*) $R_\theta = 1360$; (*b*) 2180; (*c*) 6030; (*d*) 9630.

corroboration of our choice for U_c, it is neither an objective nor an accurate way of determining U_c. An illustration of the difficulty is provided by figure 4 which shows streamlines, calculated for two values of U_c ($0.7U_1$ and $0.8U_1$) from the same experiment but using a different part of the record than that of figure 3. Foci F_3 and F_4 which appear at relatively large y/δ (figure 4*b*, $U_c = 0.8U_1$) are absent in figure 4(*a*) ($U_c = 0.7U_1$). Foci F_1 and F_2 which are present at relatively small values of y/δ in figure 4(*a*) do not appear in figure 4(*b*). Foci F_5 and F_6 appear in both figures 4(*a*) and 4(*b*). All the foci in figures 4(*a*) and 4(*b*) are associated with relatively important magnitudes of ω_z (figure 4*c*), although the association is not always perfect, possibly because of the smoothing involved in forming ω_z. Contours of γ, an approximation to the rate of strain, viz. $\gamma = -\bar{U}^{-1}\partial V/\partial t + \partial U/\partial y$, are shown in figure 4(*d*). As for ω_z, the present estimates of γ are attenuated as a result of probe separation and should only be interpreted as approximations to the rate of strain associated with a large-scale motion. Like ω_z, γ does not depend on U_c and can therefore be interpreted less ambiguously than streamlines.

It is difficult to gain insight into the three-dimensional vortical structure of the flow using information obtained in only one plane. Nevertheless, the present patterns contain features similar to those obtained by Robinson *et al.* (1989) in a three-dimensional numerical simulation of a turbulent boundary layer. For example, the patterns near foci F_5 and F_6 (local concentrations of ω_z are associated with these points, figure 4*c*) are reminiscent of those associated with the roll-up of near-wall shear layers, as discussed by Robinson *et al.* These authors found that the local maximum in ω_z corresponded with a minimum in the pressure fluctuation. The spatial distribution of low-pressure regions suggested the presence of arch-like vortical structures of a broad range of sizes.

Instantaneous streamlines (figure 5) indicate few differences between $R_\theta = 1360$ (figure 5*a*) and $R_\theta = 9630$ (figure 5*d*). Independently of R_θ, the patterns tend to suggest a relatively complicated fluid motion with a diversity of lengthscales, sizes and locations of ω_z concentrations.

4. Conditional averages

To quantify the effect of R_θ on features of the organized motion, the velocity data at the four Reynolds numbers were conditionally sampled and averaged. The detection was based on u, the selection of u rather than v being partly suggested by the extent of the u-correlation contours presented in I but primarily by our previous experience in detecting temperature fronts (coolings or heatings) in the boundary layer over a slightly heated wall, e.g. Subramanian *et al.* (1982); Antonia *et al.* (1988); Antonia & Fulachier (1989). As noted in previous work, these large-scale temperature changes are accompanied by concomitant changes in u (the δ-scale u-discontinuity of Kline 1989) and by less definite changes in v. The present detection method bears similarity to several algorithms which focus on the strong acceleration of u. Examples of such algorithms are the u-level method (Bogard & Tiederman 1986) and the pattern-recognition (P-R) method of Wallace, Brodkey & Eckelmann (1977), which recognizes a gradual deceleration followed by a sudden acceleration in u. Reasonable correspondence has been found between the present method and u-level (see §5). No comparison has been made with P-R but in the light of the results of Brodkey *et al.* (1985) and Bogard & Tiederman (1986) one would expect P-R to also detect the δ-scale u-discontinuity with high probability. One of the difficulties with P-R, as reported by Bogard & Tiederman (1986) in their comparison of several detection methods with visual ejections, is that its probability of making false detections is high relative to other methods.

The window average gradient (WAG) detection scheme used here searches for changes in average signal level over a certain time interval. The change can be specified as either an increase or a decrease; an increase was always used for the present work. A computation window of length $2\tau + 1$ points is moved point by point through the data u_i ($i = 1, \ldots, N$, where N is the total number of samples, here equal to 128000, independently of R_θ) and

$$\mathrm{WAG}_i = \frac{sign}{2\tau}\left(\sum_{j=i+1}^{i+\tau} u_j - \sum_{j=i-\tau}^{i-1} u_j\right).$$

A detection region begins when WAG_i first exceeds $k\overline{u^2}^{\frac{1}{2}}$ (k is the threshold parameter) and ends when WAG_i next becomes negative. The detection point is the point of largest WAG_i within the detection region. The value of *sign* is $+1$ or -1 for detection of increases or decreases, respectively, in the signal level. The parameters k and τ were selected in order to detect the nearly simultaneous increases in the u-signals of the array. An example of detections, indicated by arrows, is given in figure 6. Values of 0.45 and 0.9 were used for k and $\tau U_1/\delta$ respectively. While this selection is arbitrary, the present conditional data were found to be relatively insensitive to the choice of k and τ.

Although the WAG criterion is applied separately to each u-signal, the detections tend to appear in distinct groups (figure 6). Detections generally occur earlier at larger y/δ, consistent with the inclination to the wall of the large-scale motion. Probability density functions of the intervals between consecutive detections at all

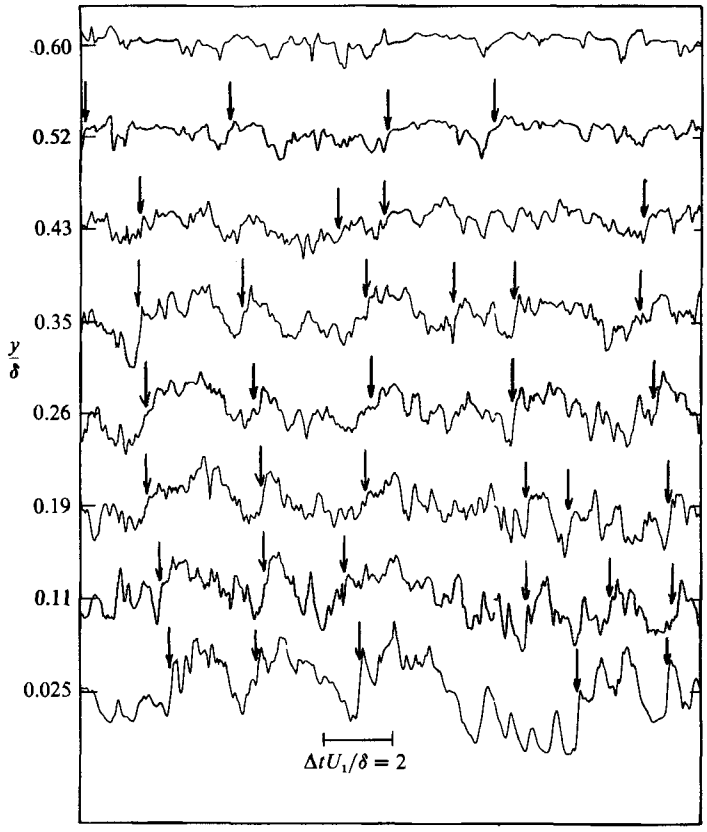

FIGURE 6. Traces of u-signals at $R_\theta = 2180$. Note that $\Delta tU_1/\delta = 2$ is approximately the magnitude of the WAG window. Downward arrows represent WAG detection locations. Time increases left to right.

probe locations $y/\delta \leqslant 0.6$ were computed. These p.d.f.s indicated that the interval T_p corresponding to the maximum of the p.d.f. remained approximately constant ($\approx 2.5\delta/U_1$) with Reynolds number although the curves have a relatively broad peak (figure 7). The value of T_p lies within the range found by Fleischmann & Wallace (1984) for the mean period of organized structures in bounded turbulent flows.

Conditional averages were formed using only those segments of the digital record that contained two detections which were separated by an interval of time equal to T_p ($\pm 10\%$). This strategy, although not the only possible one, should reduce the jitter in the structures for the purpose of comparing results at different R_θ, while retaining a sufficient number of detections for conditional averaging. The y-location ($\approx 0.25\delta$) at which detections were made was just below the centre of the array when the latter was nearest the wall. Conditional averages are denoted by an angular bracket, viz.

$$\langle f \rangle = \frac{1}{n}\sum_{i=1}^{n} f(t_i + \Delta t),$$

where the time delay Δt is measured relative to the detection instant t_i and n is the number of detections (it varied from 59 at $R_\theta = 1360$ to 309 at $R_\theta = 9630$).

The conditional streamlines of figure 8(a, d, g, j) have two saddle points at $\Delta x/\delta = 0$ and $\Delta x/\delta \approx -2$ ($\Delta tU_1/\delta \approx 2.5$). Foci occur half-way between these points, but, unlike the instantaneous results in figure 3, the foci do not correspond with

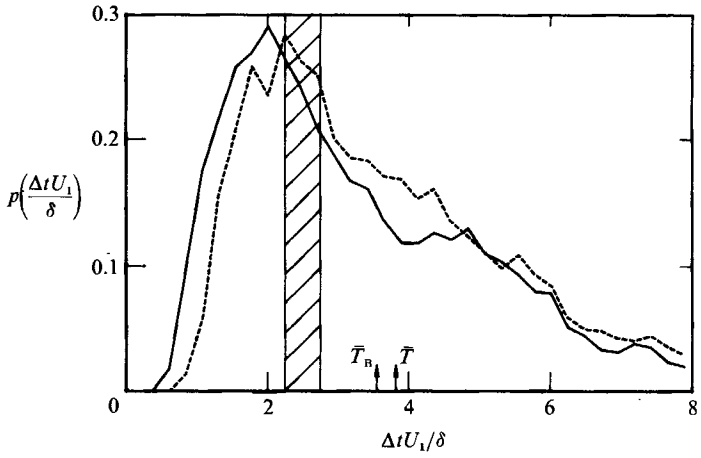

FIGURE 7. Probability density functions of the periods between WAG detections and between burst detections, as determined by the modified u-level method. Arrows indicate average values of the periods. The hatched region defines the subset of detections used for the conditional data. $R_\theta = 2180$. ——, burst detections: – – –, WAG detections.

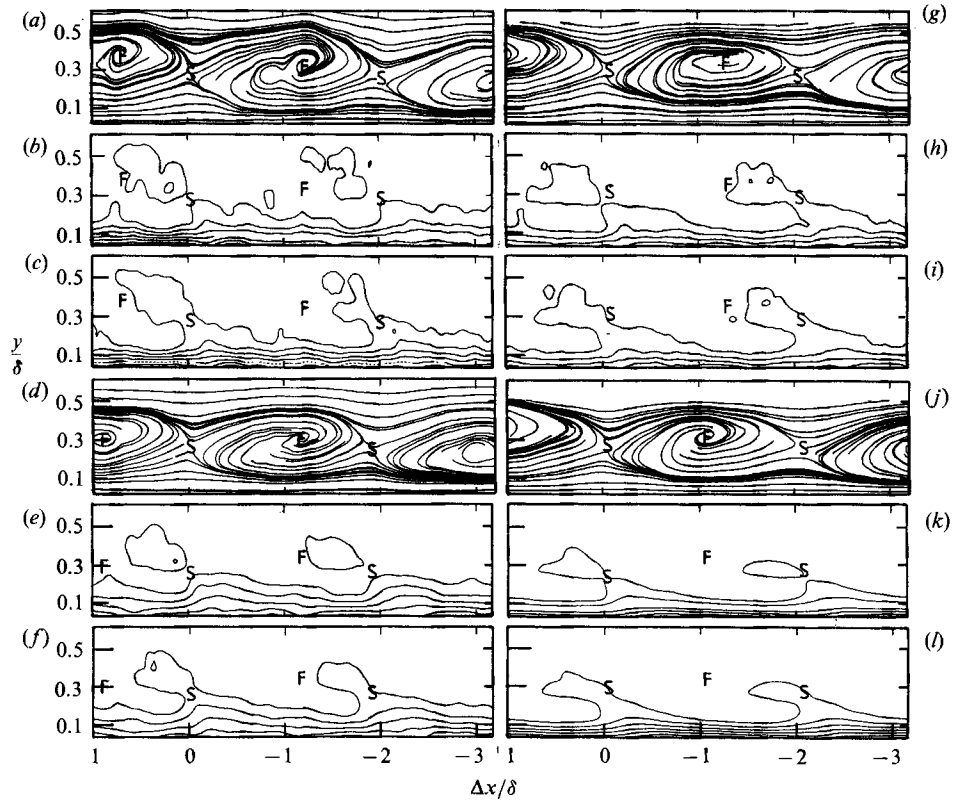

FIGURE 8. Conditional streamlines, large-scale spanwise vorticity and strain rate contours in the region $0 \leqslant y/\delta \lesssim 0.6$. The frame of reference translates to the left with $U_c = 0.8U_1$. Streamlines: (*a*) $R_\theta = 1360$; (*d*) 2180; (*g*) 6030; (*j*) 9630. Spanwise vorticity: (*b*) $R_\theta = 1360$; (*e*) 2180; (*h*) 6030; (*k*) 9630. Strain rate: (*c*) $R_\theta = 1360$; (*f*) 2180; (*i*) 6030; (*l*) 9630. The outermost vorticity contour value is $-0.7U_1/\delta$ and the contour step is $-0.5U_1/\delta$; the corresponding values for strain rate are $0.7U_1/\delta$ and $0.5U_1/\delta$.

regions of highest spanwise vorticity. Contours of $\langle\omega_z\rangle$ (figure 8*b*, *e*, *h*, *k*) indicate concentrations along the diverging separatrices† below the saddle and downstream of these separatrices above the saddle, the highest values of $\langle\omega_z\rangle$ occurring near the wall. Comparison between the streamlines in figures 5 and 8 illustrates the change of emphasis that results from conditional averaging. Only those patterns which are associated with the narrow band of lengthscales defined in figure 7 emerge in figure 8.

The conditional streamlines in figure 8 are qualitatively similar to those obtained for a turbulent boundary layer by Brown & Thomas (1977), Antonia & Fulachier (1989), and those computed by Kim (1985) from data obtained from a large-eddy simulation of turbulent channel flow. The similarity, despite the effect of U_c and the choice of the detection location, is worth noting since slightly different methods of detection were used in the different investigations.

Figure 8(*b*, *e*, *h*, *k*) indicates that contours of constant $\langle\omega_z\rangle\delta/U_1$ extend to larger values of y/δ at lower Reynolds numbers, e.g. the -0.7 contour reaches $y/\delta = 0.55$ for $R_\theta = 1360$ but only $y/\delta = 0.35$ at $R_\theta = 9630$. There is a close similarity between $\langle\gamma\rangle$ (figure 8*c*, *f*, *i*, *l*) and $\langle\omega_z\rangle$, except that contours of $\langle\gamma\rangle$ usually go through or include the saddle points. In particular, the lowest contours extend further away from the wall as R_θ decreases while their inclination to the wall increases. There is a possible explanation for the apparent dependence on R_θ of the $\langle\omega_z\rangle$ (or $\langle\gamma\rangle$) contours. The concentration of ω_z occurs all along the strong internal shear layer in the near-wall zone. Using direct numerical simulation data for a turbulent channel flow at a relatively small Reynolds number, Kim (1988) associated this shear layer with the upstream edge of the inclined large-scale motion. When R_θ is small, there should be relatively little difference between the wall lengthscales responsible for most of the turbulent energy production and the outer lengthscales. As R_θ increases, this distinction becomes more marked and consequently the concentrations of $\langle\omega_z\rangle$ and $\langle\gamma\rangle$ tend to lie closer to the wall. The poor correspondence between foci and $\langle\omega_z\rangle$ concentrations may be due in part to the detection criterion not focusing directly on the spanwise vorticity but also to the fact that, instantaneously, foci are observed over a wide range of distances from the wall and do not necessarily lie immediately upstream of diverging separarices.

5. Relationship between the outer motion and wall bursting

To detect bursts, use was made of the method outlined by Luchik & Tiederman (1987). These authors modified a scheme, originally introduced by Lu & Willmarth (1973), in which the beginning of an ejection is considered to occur when

$$u < -L\overline{u^2}^{\frac{1}{2}},$$

where L is a dimensionless threshold parameter. The ejection ends when

$$u \geqslant -0.25L\overline{u^2}^{\frac{1}{2}}.$$

The dual threshold was introduced to eliminate multiple detections of a single ejection. To group ejections from a single burst, we have followed the approach of Barlow & Johnston (1988) and Tiederman (1989). The grouping time (or minimum acceptable time interval between the end of one ejection and the beginning of the next) is identified with the intersection of two linear segments on a semi-log plot of the cumulative probability for this time interval. Grouping is important since a

† Their direction is easily inferred from that of the streamlines near the saddle positions.

threshold-independent number of bursts (or grouped ejections) is found only after grouping.

The detection scheme, as outlined above with the grouping procedure of Tiederman (1989), was applied to the u-signal from the $\times$-probe closest to the wall. This was done only for $R_\theta = 1360$ and 2180 since y^+ was approximately 15 for this probe location and the wire length was sufficiently small (less than 20 wall units, cf. table 1) for these two Reynolds numbers. A range of L (typically 0.2 to 0.7) was found for which $\bar{T}_B$, the average period between bursts, was practically constant. A final value of 0.6 was used for L. The resulting values of $\bar{T}_B$ were found to be equal to 5.8 and $3.2\delta/U_1$ corresponding to grouping times of $1.2\delta/U_1$ ($R_\theta = 1360$) and $0.6\delta/U_1$ ($R_\theta = 2180$). (The corresponding values of $\bar{T}_B^+$ are 136 and 103 respectively. This is consistent with Shah & Antonia's (1989) suggestion that scaling on wall variables is relevant at relatively small Reynolds number – up to $R_\theta \approx 5000$.) These values of $\bar{T}_B$ are in good agreement with those obtained by Shah & Antonia (1989) in the same flow, also for $y^+ = 15$, with a single hot wire about 2 wall units long. Probability density functions of T_B, obtained with the $\times$-probe and with the single hot wire, were nearly identical. Values of $\bar{T}$, the average period between WAG detections, are in reasonable agreement with $\bar{T}_B$ (figure 7 for $R_\theta = 2180$). Note that $\bar{T}$ is significantly larger than the value of 2.5 for T_p, the most probable period between detections.

The agreement between $\bar{T}$ and $\bar{T}_B$, or between $p(T)$ and $p(T_B)$ (figure 7) implies a connection between the WAG detections and bursting. This is of interest in terms of establishing a possible association between wall bursts and a motion on the scale of the boundary-layer thickness (a feature of this motion is the δ-scale u-discontinuity). A measure of the correspondence between T and T_B is provided by the relative probabilities of the time between either the beginning or end of a burst, as identified by detections using the modified u-level method, and the occurrence of the δ-scale u-discontinuity, as identified by WAG detections. Both detection methods were applied at $y^+ = 15$. Taking the WAG detection to be at $\Delta t = 0$, figure 9(*a*) shows that the most probable location of the beginning of a burst is of order 0.5δ to 1.0δ downstream of the WAG detection. By contrast, the end of a burst (figure 9*b*) has a maximum probability near $\Delta t = 0$. The range $\pm 0.19\delta/U_1$, indicated in figure 9(*b*), accounts for 61% and 60% of all bursts detected at $R_\theta = 1360$ and $R_\theta = 2180$ respectively.

It is of interest to examine the structure of the uv-signal near the end of a burst. Conditional averages of uv, conditioned on the end of a burst, were computed at $y^+ = 15$ for $R_\theta = 1360$ and 2180. These distributions are shown in figure 10 together with distributions of $\langle u\rangle\langle v\rangle$. The difference between $\langle uv\rangle$ and $\langle u\rangle\langle v\rangle$ represents $\langle u_r v_r\rangle$, where u_r and v_r are the incoherent velocity fluctuations, viz. $u_r \equiv u - \langle u\rangle$ and $v_r \equiv v - \langle v\rangle$. The $\langle u\rangle\langle v\rangle$ distribution follows $\langle uv\rangle$ more closely for positive than negative values of Δt. Upstream of the detection ($\Delta t > 0$), the motion is in quadrant 4 ($u > 0$, $v < 0$) while downstream ($\Delta t < 0$) it is in quadrant 2 ($u < 0$, $v > 0$). Comparison of the $\langle uv\rangle$ and $\langle u\rangle\langle v\rangle$ distributions in figure 10 implies that the quadrant-4 (or sweep-like) motion is more coherent than the quadrant-2 (or burst-related) motion, for both values of R_θ. The area under the $\langle u\rangle\langle v\rangle$-distribution is larger at $R_\theta = 1360$ than $R_\theta = 2180$. This is qualitatively consistent with the notion that the contribution from the organized motion to $\overline{uv}$ increases as R_θ decreases.

The sequence and relative spacing of events implied by the above information conforms with the observation that internal shear layers are preceded and followed by quadrant-2 and quadrant-4 events respectively. It should be kept in mind, however, that the present Eulerian measurements are confined to the (x, y)-plane so

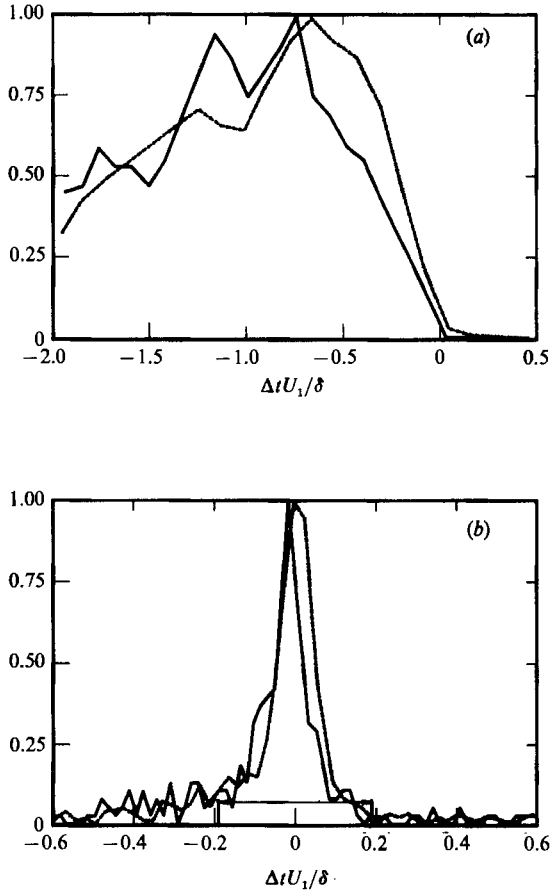

FIGURE 9. Normalized and smoothed histograms of the time between either the beginning or end of a burst, determined by the modified u-level method ($y^+ \approx 15$), and the WAG detection (at $\Delta t = 0$ and $y^+ \approx 15$). ——, $R_\theta = 1360$; - -, $R_\theta = 2180$. (a) beginnings of bursts; (b) ends of bursts.

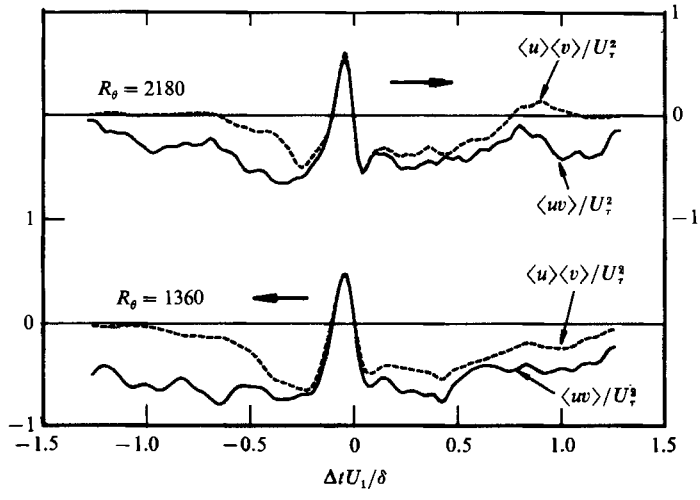

FIGURE 10. Distributions of $\langle uv\rangle/U_\tau^2$ and $\langle u\rangle\langle v\rangle/U_\tau^2$ associated with the end of a burst, detected by the modified u-level method at $y^+ \approx 15$, and $R_\theta = 1360$ and 2180. ——, $\langle uv\rangle/U_\tau^2$; - -, $\langle u\rangle\langle v\rangle/U_\tau^2$.

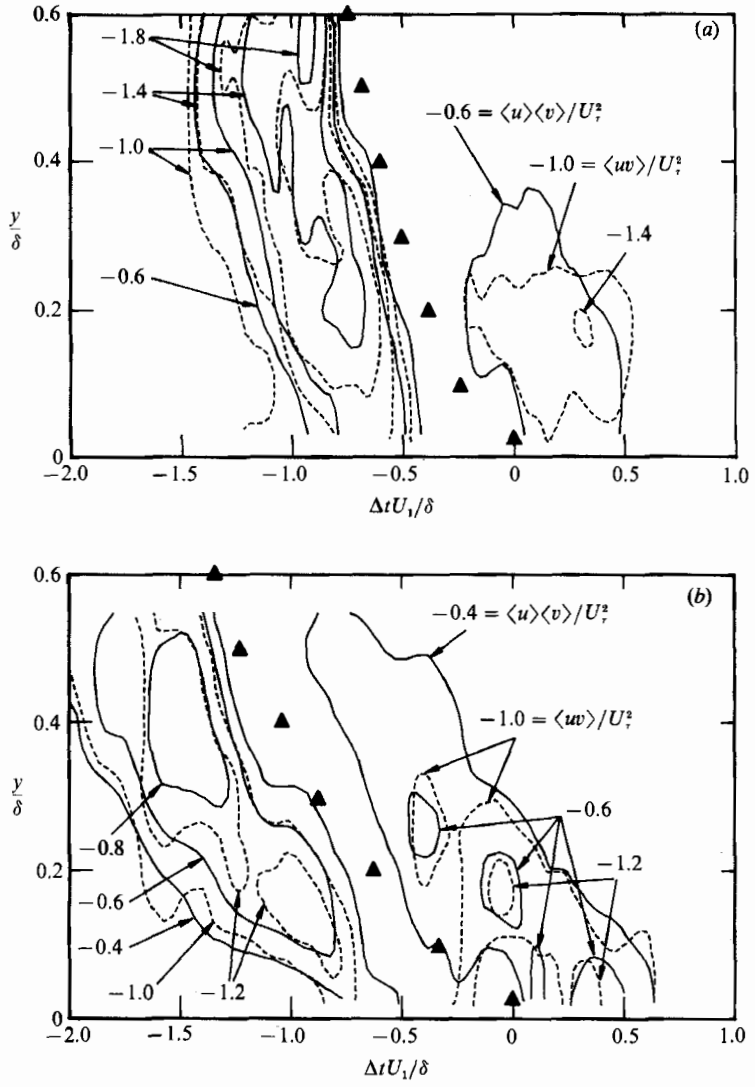

FIGURE 11. Contours of $\langle uv\rangle/U_\tau^2$ and $\langle u\rangle\langle v\rangle/U_\tau^2$ associated with the δ-scale u-discontinuity. The approximate location of the discontinuity is indicated by the filled-in triangles. (*a*) $R_\theta = 1360$; (*b*) $R_\theta = 6030$. - -, $\langle uv\rangle/U_\tau^2$; ——, $\langle u\rangle\langle v\rangle/U_\tau^2$.

that it would be difficult to draw conclusions about the possible cause or trigger for these events. The direct numerical simulations of Robinson *et al.* (1989) suggest that, in a convected frame, the sequence of events propagates through the flow with fixed relative positions in space.

Since the δ-scale u-discontinuity may be interpreted as providing a link between the near-wall bursting and the outer motion, it also seemed pertinent to investigate the structure of the uv-signal along the discontinuity. An approximate shape for the discontinuity was obtained from the preferred WAG detection positions at the various probe locations in the array. The preferred positions (triangles in figure 11) were estimated from the locations of peaks in histograms of the delay between WAG detections at a particular value of y, relative to WAG detections at a reference y. As

the difference between the two y-values increased, the reference y-location was changed so that the peak in the histogram remained well defined. The discontinuity rises more sharply from the wall at $R_\theta = 1360$ (figure 11*a*) than at $R_\theta = 6030$ (figure 11*b*). This difference reflects a similar difference between the shapes of the u-correlation contours presented in I. Contour values of $\langle uv\rangle/U_\tau^2$ and $\langle u\rangle\langle v\rangle/U_\tau^2$, associated with the discontinuity, have significantly higher values for $R_\theta = 1360$ (figure 11*a*) than $R_\theta = 6030$ (figure 11*b*). Also, $\langle u\rangle\langle v\rangle$ follows $\langle uv\rangle$ more closely at the smaller Reynolds number, further substantiating the claim that the contribution to the Reynolds shear stress is larger as R_θ decreases. Large values of $\langle u\rangle\langle v\rangle$ (and $\langle uv\rangle$) are maintained, almost independently of y/δ, in the region downstream of the discontinuity. As y/δ increases, the discontinuity should coincide with the turbulent/non-turbulent interface, thus accounting for the disappearance of the contours upstream of the discontinuity. Downstream of the discontinuity, the peak magnitude of $\langle uv\rangle$ or $\langle u\rangle\langle v\rangle$ exceeds the wall shear stress by a factor of almost two (figure 11*a*). This implies that information about the wall shear stress is efficiently conveyed to the outer region along the discontinuity, especially at smaller R_θ.

6. Topology of the outer layer

Data from the $\times$-probe array, when the latter covered the region $0.6 \lesssim y/\delta \lesssim 1.1$, were treated in similar fashion to the data obtained closer to the wall. One obvious advantage, however, in dealing with velocity information in the outer part of the layer is that the mean velocity variation in this region is quite small. As in the case of the far wake (e.g. Antonia *et al.* 1987), this means that streamlines are less sensitive to the choice of U_c. The streamlines in figure 12 are displayed in a frame of reference that translates in the flow direction with $U_c = 0.95U_1$. This value is close to that ($0.93U_1$) used by Blackwelder & Kovasznay (1972) to obtain a composite velocity distribution in the outer region of the boundary layer.

Figure 12 was obtained by applying the WAG detection method to the u-signal at $y/\delta \approx 0.7$. As in §4, a set of detections with the most probable time separation was selected; the value of $T_p U_1/\delta$ was 2.5, at all R_θ, as in the case of $y/\delta \approx 0.25$ (figure 8). One feature of figure 12 is the variation in the curvature of streamlines with Reynolds number. At $R_\theta = 1360$ the foci are more nearly circular and tend to protrude slightly further into the free stream than at higher Reynolds numbers. Also, the locations of the foci are higher at $R_\theta = 1360$ ($y/\delta = 0.83$) than at $R_\theta = 9630$ ($y/\delta = 0.78$). The behaviour of the streamlines at $R_\theta = 1360$ seems consistent with that observed when the array is nearer the wall. It also seems consistent with the flow photographs of Fiedler & Head (1966) which suggest that the turbulent/non-turbulent interface is more re-entrant at $R_\theta = 1000$ than at $R_\theta = 5000$.

The low-level (-0.2) contour of $\langle\omega_z\rangle$ in figure 12 does not change substantially with R_θ. More importantly, this contour encompasses the foci quite well. The stronger contours (-0.4 and -0.6) generally lie upstream of the foci (near the upstream end of the large bulges). The peak magnitudes of $\langle\omega_z\rangle$ in figure 12 are, as expected, smaller than those obtained closer to the wall (figure 8). There is obvious similarity between the topology of figure 12 and that obtained (Antonia *et al.* 1987) in the cylinder far wake (on one side of the centreline). It is reasonable to associate the -0.2 vorticity contour in figure 12 with the slowly overturning motion which is seen in flow visualizations and has been inferred from conditional hot-wire data in the outer layer (e.g. Kovasznay, Kibens & Blackwelder 1970; Antonia 1972). It would be imprudent, however, to interpret this in terms of a single large-scale

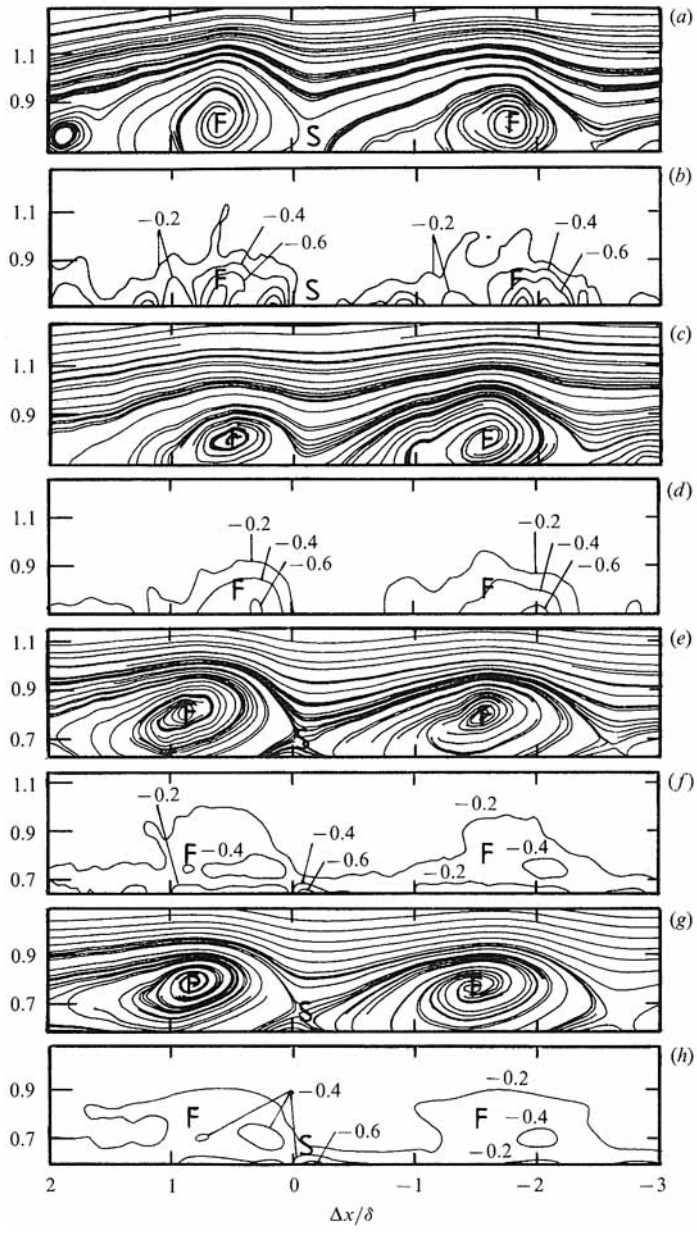

FIGURE 12. Conditional streamlines and large-scale spanwise vorticity contours in the outer layer. The frame of reference translates to the left with $U_c = 0.95U_1$. Streamlines: (*a*) $R_\theta = 1360$; (*c*) 2180; (*e*) 6030; (*g*) 9630. Spanwise vorticity: (*b*) $R_\theta = 1360$; (*d*) 2180; (*f*) 6030; (*h*) 9630. The outermost vorticity contour value is $\omega_z \delta/U_1 = -0.2$ and the contour step is -0.2.

vortical structure because of the possible smearing of signatures of individual structures within large-scale bulges due to conditional averaging. The possibility that bulges are made up of an agglomeration of structures, as conjectured in the context of the wake (Antonia *et al.* 1987), cannot be excluded.

7. Conclusions

Using an array of $\times$-probes in the (x, y)-plane, the topology of the boundary layer has been obtained both instantaneously and conditionally, at four values of R_θ.

The instantaneous streamline patterns and contours of approximations to the large-scale spanwise vorticity and strain rate suggest that the flow structure is relatively complicated, independently of R_θ. The conditional patterns extend further from the wall as R_θ decreases. In the outer part of the layer, these patterns are similar to those previously obtained in the far wake of a cylinder.

In the wall region, reasonable correspondence exists between δ-scale u-discontinuities and the upstream ends of the bursts. The discontinuities extend from the wall to the outer edge of the layer, thus providing a possible link between bursting and the outer larger-scale motion. The Reynolds shear stress associated with the discontinuities is significant throughout the layer. The coherent contribution to this stress is larger at smaller Reynolds numbers, a result consistent with the similarity, at these Reynolds numbers, between the lengthscale of the outer motion and that of the Reynolds stress carrying motion near the wall.

The support of the Australian Research Grants Scheme is gratefully acknowledged. We wish to thank Dr D. A. Shah for his assistance with the experiments.

REFERENCES

ALFREDSSON, P. H. & JOHANSSON, A. V. 1984 *Phys. Fluids* **27**, 1974–1981.

ANDREOPOULOS, J., DURST, F., ZARIC, Z. & JOVANOVIC, J. 1984 *Expts Fluids* **2**, 7–16.

ANTONIA, R. A. 1972 *J. Fluid Mech.* **56**, 1–18.

ANTONIA, R. A., BROWNE, L. W. B. & BISSET, D. K. 1989 In *Near-Wall Turbulence: 1988 Zoran Zaric Memorial Conference*. Hemisphere (referred to as I).

ANTONIA, R. A., BROWNE, L. W. B., BISSET, D. K. & FULACHIER, L. 1987 *J. Fluid Mech.* **184**, 423–444.

ANTONIA, R. A. & FULACHIER, L. 1989 *J. Fluid Mech.* **198**, 429–451.

ANTONIA, R. A., FULACHIER, L., KRISHNAMOORTHY, L. V., BENABID, T. & ANSELMET, F. 1988 *J. Fluid Mech.* **190**, 217–240.

ANTONIA, R. A., RAJAGOPALAN, S., SUBRAMANIAN, C. S. & CHAMBERS, A. J. 1982 *J. Fluid Mech.* **121**, 123–140.

BARLOW, R. S. & JOHNSTON, J. P. 1988 *J. Fluid Mech.* **191**, 177–195.

BLACKWELDER, R. F. & KOVASZNAY, L. S. G. 1972 *Phys. Fluids* **15**, 1545–1554.

BOGARD, D. G. & TIEDERMAN, W. G. 1986 *J. Fluid Mech.* **162**, 389–413.

BRODKEY, R. S., AOUAD, Y. G., VALIZADEH-ALAVI, H. & ECKELMANN, H. 1985 In *Flow of Real Fluids*. Lecture Notes in Physics, vol. 235, pp. 279–291. Springer.

BROWN, G. L. & THOMAS, A. S. W. 1977 *Phys. Fluids* **20**, S243–S252.

BROWNE, L. W. B., ANTONIA, R. A. & CHUA, L. P. 1989 *Expts Fluids* **8**, 13–16.

CHEN, C.-H. P. & BLACKWELDER, R. F. 1978 *J. Fluid Mech.* **89**, 1–31.

COLES, D. 1962 *Rand Corp. Rep.* R-403-PR, ARC 24478.

COLES, D. 1982 In *Surveys in Fluid Mechanics* (ed. R. Narasimha & S. M. Deshpande), pp. 17–33. Bangalore: Indian Academy of Sciences.

ERM, L. P., SMITS, A. J. & JOUBERT, P. N. 1987 In *Turbulent Shear Flows 5* (ed. F. Durst, B. E. Launder, J. L. Lumley, F. W. Schmidt & J. H. Whitelaw), pp. 186–196. Springer.

FALCO, R. E. 1974 *AIAA Paper* 74-99, presented at AIAA 12th Aerospace Sciences Meeting, Washington.

FALCO, R. E. 1977 In *Turbulence in Internal Flows* (ed. S. N. B. Murthy), pp. 113–130. Hemisphere.

FALCO, R. E. 1980 *Trans. ASME* I: *J. Fluids Engng* **102**, 174–182.

FIEDLER, H. & HEAD, M. R. 1966 *J. Fluid Mech.* **25**, 719–735.

FLEISCHMANN, S. T. & WALLACE, J. M. 1984 *AIAA J.* **22**, 766–769.

HEAD, M. R. & BANDYOPADHYAY, P. 1981 *J. Fluid Mech.* **107**, 297–338 (referred to as HB).

HUSSAIN, A. K. M. F. 1986 *J. Fluid Mech.* **173**, 303–356.

KIM, J. 1985 *Phys. Fluids* **28**, 52–58.

KIM, J. 1988 In *Transport Phenomena in Turbulent Flows* (ed. M. Hirata & N. Kasagi), pp. 715–729. Hemisphere.

KLEBANOFF, P. S. 1955 *NACA Rep.* 1247.

KLINE, S. J. 1989 In *Near-Wall Turbulence*: *1988 Zoran Zaric Memorial Conference*. Hemisphere.

KOVASZNAY, L. S. G., KIBENS, V. & BLACKWELDER, R. F. 1970 *J. Fluid Mech.* **41**, 283–325.

LU, S. S. & WILLMARTH, W. W. 1973 *J. Fluid Mech.* **60**, 481–512.

LUCHIK, T. S. & TIEDERMAN, W. G. 1987 *J. Fluid Mech.* **174**, 529–552.

MURLIS, J., TSAI, H. M. & BRADSHAW, P. 1982 *J. Fluid Mech.* **122**, 13–56.

PERRY, A. E. & CHONG, M. S. 1987 *Ann. Rev. Fluid Mech.* **19**, 125–155.

PIOMELLI, U., BALINT, J.-L. & WALLACE, J. M. 1989 *Phys. Fluids* A **1**, 609–611.

PURTELL, L. P., KLEBANOFF, P. S. & BUCKLEY, F. T. 1981 *Phys. Fluids* **24**, 802–811.

ROBINSON, S. K., KLINE, S. J. & SPALART, P. R. 1989 In *Near-Wall Turbulence*: *1988 Zoran Zaric Memorial Conference*. Hemisphere.

SHAH, D. A. & ANTONIA, R. A. 1989 *Phys. Fluids* A **1**, 318–325.

SMITH, C. R. & METZLER, S. P. 1983 *J. Fluid Mech.* **129**, 27–54.

SPALART, P. R. 1988 *J. Fluid Mech.* **187**, 61–98.

SUBRAMANIAN, C. S. & ANTONIA, R. A. 1981 *Intl J. Heat Mass Transfer* **24**, 1833–1846.

SUBRAMANIAN, C. S., RAJAGOPALAN, S., ANTONIA, R. A. & CHAMBERS, A. J. 1982 *J. Fluid Mech.* **123**, 335–362.

TIEDERMAN, W. G. 1989 In *Near-Wall Turbulence*: *1988 Zoran Zaric Memorial Conference*. Hemisphere.

TOWNSEND, A. A. 1956 *The Structure of Turbulent Shear Flow*. Cambridge University Press.

WALLACE, J. M. 1984 In *Turbulence and Chaotic Phenomena in Fluids* (ed. T. Tatsumi), pp. 447–452. North-Holland.

WALLACE, J. M., BALINT, J.-L., MARIAUX, J.-L. & MOREL, R. 1983 In *Recent Advances in Engineering Mechanics and Their Impact on Civil Engineering Practice* (ed. W. F. Chen & A. D. M. Lewis), pp. 1198–1201. Purdue University.

WALLACE, J. M., BRODKEY, R. S. & ECKELMANN, H. 1977 *J. Fluid Mech.* **83**, 673–693.

WILLMARTH, W. W. 1978 In *Workshop on Coherent Structure of Turbulent Boundary Layers* (ed. C. R. Smith & D. E. Abbott), pp. 130–162. Lehigh University.